

Content

Abstract (in Chinese).....	i
Abstract (in English).....	ii
Acknowledgement.....	iii
Content.....	v
Table Caption.....	vii
Figure Caption.....	viii
Chapter 1 Introduction.....	1
1.1 Overview.....	1
1.2 Outline of this dissertation.....	3
Chapter 2 GaN-Based Micro-Hole Array Light-Emitting Diodes.....	5
2.1 Progress in GaN-based micro-structure LEDs.....	5
2.2 Design and simulation of micro-hole array LEDs.....	6
2.3 Fabrication of GaN-based micro-hole array LEDs.....	7
2.4 Characteristics of GaN-based micro-hole array LEDs.....	8
Chapter 3 InGaN Quantum Dots Grown on SiN Nanoholes.....	22
3.1 Introduction.....	22
3.2 Experiment setup and sample growth.....	24
3.3 Photoluminescence of InGaN QDs.....	26
3.4 Thermal annealing effects on optical properties of the InGaN QDs.....	27
Chapter 4 InGaN/GaN Multiple Quantum Wells Nanorods.....	39
4.1 Introduction.....	39
4.2 Dry etching of III-Nitride materials.....	39
4.3 Fabrication of InGaN/GaN MQWs nanorods.....	42
4.4 Optical properties of the InGaN/GaN MQWs nanorods.....	47
Chapter 5 Effects of Delta-Trimethylindium-Flow Process on Optical Properties of InGaN/GaN Multiple Quantum Wells.....	68
5.1 Introduction.....	68
5.2 Experiments.....	68

5.3 Temperature-dependent photoluminescence.....	71
5.4 Photoluminescence excitation and light output performance.....	73
Chapter 6 Summary.....	85
Publication List.....	87
Curriculum Vita.....	89



Table Caption

Table 2.1 Parameters for the light-tracing simulation of micro-hole array LEDs.

Table 3.1 Summary of growth condition, PL peak energy and QDs height for InGaN QDs.

Table 5.1 Summary of the x-ray result for sample A and B.



Figure Caption

Chapter 2

Fig. 2.1 Schematics of (a) the MQW structure and (b) the MQW microdisks. A top view SEM image of the microdisk structure is shown in (c).

Fig. 2.2 Temperature dependence of the A-exciton decay lifetime (τ) up to 100 K. Open squares represent the MQWs and closed triangles represent the microdisks.

Fig. 2.3 Optical microphotographs of (a) 16×16 micro-LED array (the image is 0.9 mm on a side) and (b) 64×64 array (2.4 mm on a side).

Fig. 2.4 (a) SEM and (b) optical microscope images of one of our interconnected μ -disk LEDs fabricated from InGaN/GaN QW structures. As illustrated in these images, about 200 μ -disk are interconnected and fit into an area of $300 \times 330 \mu\text{m}^2$.

Fig. 2.5 (a) Schematic of μ -disk LEDs based on p-GaN/InGaN/n-GaN QWs. (b) Optical microscope image (top view) of a microdisplay fabricated from an individually addressed m-disk LED array. The dimension of the microdisplay is $0.5 \times 0.5 \text{ mm}^2$ (made up of 10×10 pixels, $12 \mu\text{m}$ in diameter). [12]

Fig. 2.6 (a) Schematics of the design of a microring LED and (b) diagram showing the possible light extraction pathways from a microring geometry.

Fig. 2.7 (a) Cross-sectional schematic of the device structure, and (b) microscope image of the operating device showing four pixels turned on at 6 V.

Fig. 2.8 Diagrams of extraction efficiency for the conventional LEDs.

Fig. 2.9 Irradiance map of a conventional LED with device dimension of $360 \times 250 \mu\text{m}^2$ simulated from the Trace Pro program.

Fig. 2.10 Showing the process flowchart of the GaN-based micro-hole array LEDs.

Fig. 2.11 Cross-sectional SEM image of the micro-hole array LED.

Fig. 2.12 Optical microscope image of a $360 \mu\text{m} \times 250 \mu\text{m}$ micro-hole array LED with $d = 7 \mu\text{m}$. (b) schematic diagram of a representative micro-hole array LED fabricated by

photolithography patterning and dry etching.

Fig. 2.13 Diagram of Electrical measurement system.

Fig. 2.14 Curves of current-voltage (I - V) of micro-hole array LEDs and a conventional BA LED fabricated from the same wafer. The insert is the current density-voltage (J - V) curves of the devices.

Fig. 2.15 Light output power of micro-hole array LEDs and a conventional BA LED as functions of injected current density. The insert shows the light output power-current (L - I) curves.

Fig. 2.16 Showing (a) micro-photograph and (b) emission profile of a micro-hole array LED with $d = 7 \mu\text{m}$ at 1 mA driving current.

Fig. 2.17. Schematic of light extraction in BA and micro-hole array LEDs.

Fig. 2.18. Showing the calculation enhancement of light output power from the micro-hole array LEDs (simulation) and the γ , as functions of d .

Chapter 3

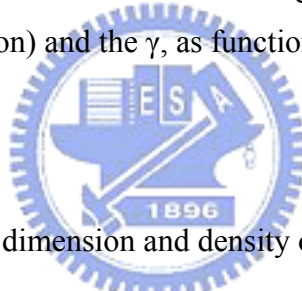


Fig. 3.1. The relation between dimension and density of states.

Fig. 3.2. A brief history of research on QD lasers particularly at the initial stage.

Fig. 3.3. A diagram of strain relaxation for S-K growth mode.

Fig. 3.4. A SEM bird's-eye-view and cross-sectional view of InGaN QD structures.

Fig. 3.5. SEM bird's-eye-view and cross-sectional view of InGaN QD structures.

Fig. 3.6. Setup diagram of the He-Cd photoluminescence measurement system.

Fig. 3.7. Setup diagram of the photoluminescence excitation measurement.

Fig. 3.8. $1 \mu\text{m} \times 1 \mu\text{m}$ AFM images of samples QD-200, QD-240 and QD-315.

Fig. 3.9. Normalized PL spectra for QD-200, Qd-240 and QD-315 at 10K.

Fig. 3.10. The PL peak shift energy for samples of QD-200, QD-240 and QD-315.

Fig. 3.11. Arrhenius plot of normalized PL intensity as a function of temperature for samples QD-200, 240, 314.

Fig. 3.12. Normalized PL spectra from samples A, B, and C at RT.

Fig. 3.13. Arrhenius plots of integrated PL intensity versus the inverse temperature for samples A, B and C.

Chapter 4

Fig. 4.1. Schematic diagram of (a) RIE, (b) ECR, and (c) ICP etch platforms.

Fig. 4.2. Schematic illustration and photo of the ICP etch system.

Fig. 4.3. SEM images of the InGaN/GaN MQWs nanorods at different chamber pressures : (a) 2.5 mTorr, (b) 20 mTorr, (c) 30 mTorr, and (d) 40 mTorr.

Fig. 4.4. SEM images of InGaN/GaN MQWs nanorods at various etching time: (a) 20 s, (b) 30 s, (c) 40 s and (d) 50 s.

Fig. 4.5. SEM images of the InGaN/GaN MQWs nanorods fabricated by ICP dry etching.

Fig. 4.6. (a) Transmission electron micrograph of a single InGaN/GaN MQWs nanorod. (b) Double-crystal x-ray diffraction spectra omega/2theta scans of the InGaN/GaN MQWs nanorods.

Fig. 4.7. Formation of nanorods and pits on the GaN surface after etching in Cl₂/Ar plasma [26-28].

Fig. 4.8. Schematic processing flowchart for InGaN/GaN MQW nanorods.

Fig. 4.9. Mean dimensions and rod number density of InGaN MQW nanorods as functions of thickness of initial Ni metal film from 50 to 150 Å.

Fig. 4.10. SEM image of InGaN/GaN MQW nanorods fabricated by ICP-RIE dry etching with self-assembled Ni metal nano-masks.

Fig. 4.11. TEM image of a single InGaN/GaN MQW nanorod.

Fig. 4.12. Setup diagram of μ-photoluminescence system.

Fig. 4.13. 80K μ-PL spectra of the In_{0.25}Ga_{0.75}N/GaN MQW nanorods and as-grown MQW sample. The inset is a scanning confocal μ-PL image at RT of a cluster of nanorods at a specific energy of 2.61 eV.

Fig. 4.14. Influence of tensile and compressive stress on E-K diagram of nitride-based materials.

Fig. 4.15. Bandgap diagram of the InGaN/GaN QW (a) with and (b) without piezoelectric field effect.

Fig. 4.16. Excitation power-density dependencies of the peak energies of nanorods and as-grown bulk samples measured at 80K.

Fig. 4.17. Excitation power-density dependencies of PL emission intensity density of nanorods and as-grown bulk samples measured at 80K.

Fig. 4.18. Photoluminescence spectrum of InGaN/GaN MQWs nanorods excited under 0.9 W/cm^2 at 4K. The insert is a photoluminescence spectrum of the as-grown bulk sample.

Fig. 4.19. Excitation power dependent photoluminescence spectra of InGaN/GaN MQWs nanorods at 4K.

Chapter 5

Fig. 5.1. Schematic diagrams of $fTMI$ variation over time in InGaN QWs for samples A and B.

Fig. 5.2. HRXRD spectra for (0004) reflection from the InGaN/GaN MQW structure of (a) sample A, (b) sample B.

Fig. 5.3. Cross-sectional TEM image of the InGaN/GaN MQWs of (a) sample A, (b) sample B. The insets in (a) and (b) are the enlarged view of the whole MQWs structure.

Fig. 5.4. The normalized PL emission spectra of samples A (solid line) and B (solid circle) at 10K.

Fig. 5.5. Temperature-dependent PL spectra of sample A (left) and B (right).

Fig. 5.6. Arrhenius plots of the normalized integrated PL intensity for the InGaN-related PL emission of sample A and B over the temperature range under investigation.

Fig. 5.7. The normalized PL intensity as a function of T^{-1} for sample A and B.

Fig. 5.8. PL and PLE spectra of the InGaN/GaN MQWs of sample A and B at 10K.

Fig. 5.9. $L-I$ characteristics for the LEDs of samples A and B.